

Numerical study of flow past an impulsively started cylinder by the lattice-Boltzmann method

By YANBING LI, RICHARD SHOCK, RAOYANG ZHANG
AND HUDONG CHEN

Exa Corporation, 3 Burlington Woods Drive, Burlington, MA 01802, USA

(Received 17 November 2003 and in revised form 20 May 2004)

In this paper a systematic numerical study of flow past an impulsively started circular cylinder at low and moderate Reynolds numbers using a lattice-Boltzmann algorithmic approach is presented together with an extended volumetric boundary scheme. Results agree well with some well-known previous works. It is demonstrated that in the nearly incompressible limit, this approach is able to provide accurate direct numerical simulations of unsteady flows with curved geometry.

1. Introduction

Time-dependent flow around an impulsively started circular cylinder is known as one of the classical prototypes of unsteady hydrodynamics. Extensive efforts have been devoted to the study of the time evolution of unsteady flow characteristics such as boundary-layer development, separation, vortex formation, shedding, pressure distribution, as well as the integrated forces.

This problem is especially interesting because the early stage of the flow development reveals a range of complex and subtle phenomena. Coutanceau & Bouard (1977*a, b*) performed detailed experimental investigations at low Reynolds numbers ($Re \leq 42.8$, with $Re = U_o D / \nu$, where U_o is the free-stream velocity, D is the cylinder diameter and ν the kinetic viscosity). Major flow features such as the time evolution of the wake eddy sizes and velocity distributions along the symmetry axis behind the cylinder were measured. Later, they further extended the work to regions of moderate and high Reynolds numbers (Bouard & Coutanceau 1980). The formation and evolution of complicated secondary flow structures were observed along with the main flow structures. These experiments have provided valuable benchmark data sets for validations of computational fluid dynamics (CFD) algorithms as well as theoretical models.

In both numerical and theoretical studies, the flow is commonly described by the incompressible Navier–Stokes equations. There are two notable theoretical works found on this subject: Collins & Dennis (1973*a*) analysed the problem in terms of the boundary-layer variables and obtained a solution via an expansion in powers of time; Bar-Lev & Yang (1975) solved the vorticity equation by the method of matched asymptotic expansion and obtained a composite solution of the inner (vortical flow) and outer (potential flow) domains up to the third order in time. However, these theoretical results are only approximately valid for sufficiently short times after the impulsive start ($T \leq 1$, where T is the dimensionless time defined by $T = U_o t / R$, with $R = D/2$ being the cylinder radius) and relatively large Reynolds numbers ($Re \geq 200$). It is believed that there is no general analytic solution for such a complex flow.

Solving such a flow with simple geometry, yet complex phenomena represents a big challenge in computational fluid dynamics. Numerical difficulties come from flow separations on smooth curved geometry and steep changes of flow properties (such as the velocity and vorticity) on the surface due to the impulsive start. The nonlinear nature of this problem also poses many difficulties in terms of stability and accuracy for various numerical methods. Therefore, it has been used extensively as a classic benchmark for evaluating numerical methods.

There are numerous numerical simulations of such a flow in the literature. Most of them are based on conventional numerical methods, such as vortex methods (Smith & Stansby 1988; Chang & Chern 1991; Koumoutsakos & Leonard 1995; Ploumhans & Winckelmans 2000) and finite-difference methods (Collins & Dennis 1973*b*; Loc 1980; Loc & Bouard 1985; Wang & Dalton 1991; Anderson & Reider 1996). Most of the early numerical simulation efforts such as Collins & Dennis (1973*b*), Loc (1980), Loc & Bouard (1985), Smith & Stansby (1988), Chang & Chern (1991), Wang & Dalton (1991), are carefully reviewed by Koumoutsakos & Leonard (1995). Koumoutsakos & Leonard (1995) also proposed a specific vortex method and presented high-resolution results over a range of Reynolds numbers ($40 \leq Re \leq 9500$) together with detailed comparisons with experimental, numerical and theoretical data. Later Ploumhans & Winckelmans (2000) pointed out that this vortex method could produce a spurious vorticity flux on the surface. They modified the point-vortex strength exchange process so that the flux could be properly diffused, thus obtaining improved results. Anderson & Reider (1996) developed an explicit finite-difference scheme with accuracy up to fourth order in theory, and performed simulations of the flow for Reynolds numbers ranging from 1000 to 9500. Schneider & Farge (2002) demonstrated the use of an adaptive wavelet method for a simulation with Reynolds number $Re = 3000$. All these approaches showed results for certain representative aspects with various extents of satisfactory experimental comparison. In particular, they gave good predictions on the steep change of the drag coefficient at the onset of the impulsive start.

Among these conventional methods, the vortex method associated with the vorticity–velocity formulation of the Navier–Stokes equations has some difficulties in the specification of the boundary conditions for the impulsive start. Despite this, it is still usually regarded as one of the most suitable numerical methods for handling these types of flow, which contain strong and sensitive vortex–wall interactions (Beale & Majda 1982*a, b*; Kida & Kimura 1998). Unlike the vortex method, the finite-difference scheme often encounters difficulties in dealing with sharp gradient changes which usually leads to numerical instability or unsatisfactory accuracy (Anderson & Reider 1996). In this paper, we mainly compare our numerical results with those from vortex methods.

Recent advances in the kinetic-theory-based lattice-Boltzmann method (LBM) has made it a promising alternative CFD approach for simulation of complex fluid flows (Chen & Doolen 1997). Unlike the Navier–Stokes-based numerical methods, the LBM describes a fluid flow in terms of a discrete kinetic equation based on the particle density distribution functions, namely the lattice-Boltzmann equation (LBE). The macroscopic flow properties are direct results of the moments of these particle distribution functions. It has been shown that LBE recovers the compressible Navier–Stokes equation at the hydrodynamic limit (Chen, Chen & Matthaeus 1992; Qian, d’Humières & Lallemand 1992; Chen & Doolen 1997; Chen, Teixeira & Molvig 1997). Furthermore, in the nearly incompressible limit, the LBM recovers the incompressible Navier–Stokes equations at an error proportional to Ma^2 . The key

advantages in the LBM include parallel computation for time-dependent flows, ease of modelling various complex fluids, and physical and more straightforward handling of complicated geometries and boundary conditions (Chen, Teixeira & Molvig 1998). It has also been demonstrated as a viable and desirable approach for large-eddy simulations of turbulent flows (Chen *et al.* 2003).

There are a series of numerical benchmarks of the LBM (Chen & Doolen 1997). However, most of the careful quantitative validations have mainly involved geometries with simple rectangular-like shapes such as cavity flow or those of backward-facing steps (Hou 1995; Shock *et al.* 2002). There are also several steady-state numerical simulations of the flow around a circular cylinder with limited quantitative comparisons (Mei & Shyy 1998; Guo, Shi & Wang 2000). The first attempt, perhaps the only one so far as we know, to simulate an impulsively started flow field was made by He & Doolen (1997). To achieve enough accuracy on the surface of a circular cylinder, they introduced a pointwise LBM interpolation scheme on a cylindrical mesh. Using this second-order-accurate method, they showed time-dependent results for a few representative Reynolds numbers, such as the mean eddy sizes, the time evolution of wake lengths, separation angles, and the streamlines. However, their approach has several drawbacks. (i) It does not have exact conservations for mass and momentum owing to the pointwise interpolations. (ii) It is difficult to extend this method to general geometry situations. (iii) It is computationally expensive. In addition, in their paper some important flow properties, including the drag history, instantaneous surface vorticity and pressure distributions, as well as careful comparisons with other numerical methods are lacking. In particular, analysis on sensitive flow properties, i.e. the behaviour of the secondary-flow structures are also missing. Therefore, it is necessary to carry out a more systematic study for an LBM approach.

In this paper, we present direct numerical simulations (DNS) of a viscous flow past an impulsively started cylinder using an LBM approach (PowerFLOW4.0 α). Extensive quantitative comparisons of the numerical results with experiment, theory and other numerical methods (mainly the vortex method) are provided. The paper is arranged as follows. A description of the specific LBE used and its realization of no-slip boundary condition on curved geometry is given in §2. Section 3 gives numerical simulations including case set-up, specification of initial and boundary conditions. Detailed numerical results, analysis and comparison, as well as some discussions are given in §4, and conclusions in §5.

2. Lattice-Boltzmann equations

The common lattice-Boltzmann equation has the following form (Chen *et al.* 1991),

$$f_i(\mathbf{x} + \mathbf{c}_i \Delta t, t + \Delta t) - f_i(\mathbf{x}, t) = C_i, \quad (2.1)$$

in which f_i is the particle distribution function moving in the i th direction, according to a finite set of the discrete velocity vectors $\{\mathbf{c}_i : i = 0, \dots, b\}$. $\mathbf{c}_i \Delta t$ and Δt are space and time increments, respectively. For convenience, we choose the convention $\Delta t = 1$ in the subsequent discussions. The collision term on the right-hand side of (2.1) may have different forms which obey the basic conservation laws (such as mass, momentum conservations and so on). The simplest and also the most popular form is the Bhatnagar–Gross–Krook (BGK) approximation (Bhatnagar, Gross & Krook 1954; Chen *et al.* 1992; Qian *et al.* 1992),

$$C_i = -\frac{f_i - f_i^{eq}}{\tau}. \quad (2.2)$$

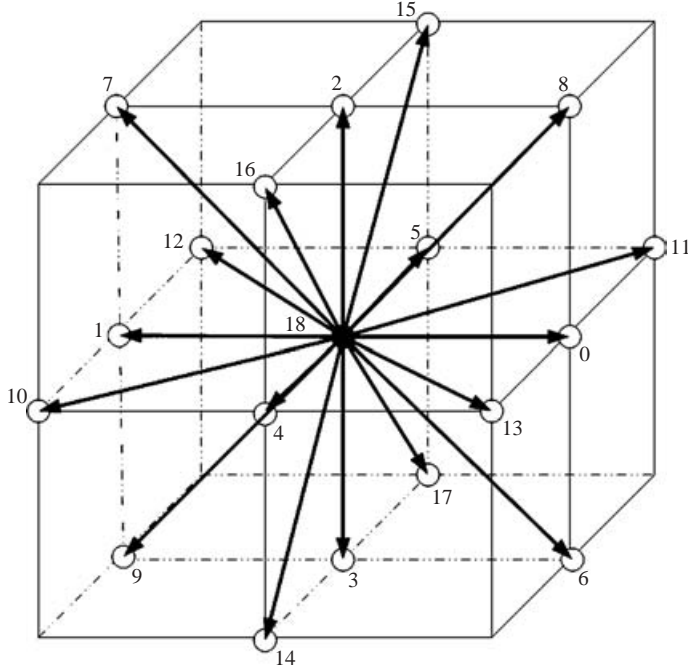


FIGURE 1. D3Q19 LBM model.

Here, τ is the single relaxation time parameter, and f_i^{eq} is the local equilibrium distribution function which depends on local hydrodynamic properties. The basic hydrodynamic quantities, such as fluid density ρ and velocity \mathbf{u} , are obtained through simple moment summations,

$$\left. \begin{aligned} \rho(\mathbf{x}, t) &= \sum_i f_i(\mathbf{x}, t), \\ \rho \mathbf{u}(\mathbf{x}, t) &= \sum_i \mathbf{c}_i f_i(\mathbf{x}, t). \end{aligned} \right\} \quad (2.3)$$

To recover macroscopic hydrodynamics, f_i^{eq} must be chosen in such a way that the essential conservation laws are satisfied and the resulting macroscopic equations are Galilean invariant. In the three-dimensional situation, one of the common choices is the D3Q19 model (Qian *et al.* 1992; Chen *et al.* 1997) shown in figure 1 with:

$$f_i^{eq} = \rho w_i \left[1 + \frac{\mathbf{c}_i \cdot \mathbf{u}}{T} + \frac{(\mathbf{c}_i \cdot \mathbf{u})^2}{2T^2} - \frac{\mathbf{u}^2}{2T} + \frac{(\mathbf{c}_i \cdot \mathbf{u})^3}{6T^3} - \frac{\mathbf{c}_i \cdot \mathbf{u}}{2T^2} \mathbf{u}^2 \right], \quad (2.4)$$

where w_i are weighting parameters:

$$w_i = \begin{cases} \frac{1}{18}, & \text{in 6 coordinate directions,} \\ \frac{1}{36}, & \text{in 12 bi-diagonal directions,} \\ \frac{1}{3}, & \text{rest particles,} \end{cases} \quad (2.5)$$

and T is the lattice temperature which is set to $1/3$ for isothermal simulations. This three-dimensional model is used in the present two-dimensional study. There are two cells in the third dimension and a periodic boundary condition is applied.

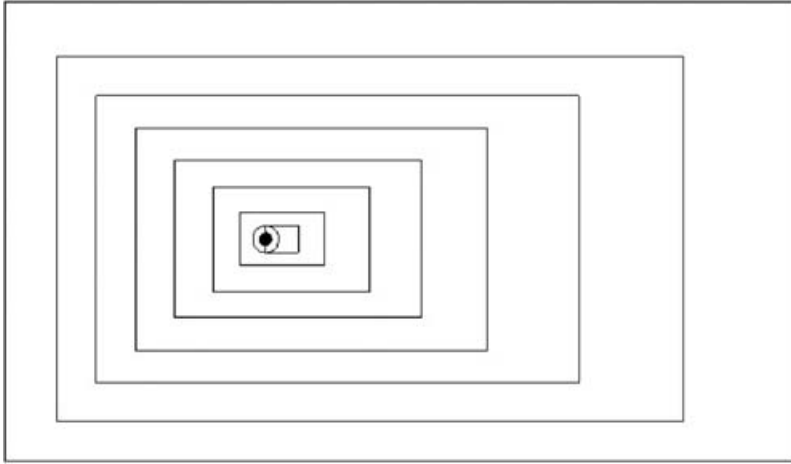


FIGURE 2. Variable resolution (VR) regions set-up for the flow past an impulsively started cylinder.

In the low-frequency and long-wavelength limit, we can recover the Navier–Stokes equations through Chapman–Enskog expansion. The resulting equation of state is that of an ideal gas, namely, the pressure p obeys a linear relation with density and temperature,

$$p = \rho T. \tag{2.6}$$

The kinematic viscosity of the fluid is related to the relaxation parameter, τ , by (Frisch, Hasslacher & Pomeau 1986; Chen *et al.* 1991, 1992, 1997; Qian *et al.* 1992)

$$\nu = \left(\tau - \frac{1}{2}\right) T. \tag{2.7}$$

It is well known that the LBM marginally satisfies the Courant–Friedrichs–Lewy condition (Chen & Doolen 1997). When τ is close to 0.5, fluid viscosity is small, and particle distributions may become negative under certain extreme situations and numerical instability may subsequently occur. To prevent the negative distribution from occurring, a simple protection procedure for ensuring positive state distributions is applied in our algorithm. That is, a local relaxation time parameter τ' in each cell is defined as the following:

$$\tau'(\mathbf{x}, t) = \max\left(\tau, 1 - \frac{f_i^{eq}(\mathbf{x}, t)}{f_i(\mathbf{x}, t)}\right), \quad \{i = 0, \dots, 18\}. \tag{2.8}$$

We can easily see that positive post-collision state distributions are guaranteed by the above as long as pre-collision distributions are positive. In other words, by effectively adding a dynamically determined viscosity lower bound, we are able to ensure positive particle distributions for all times, and thus suppress numerical instability.

In flow simulations, variable resolution (VR) regions are usually applied to achieve computation efficiency. A typical VR set-up for this study is shown in figure 2, where each bounding box represents one grid resolution level and VRs cascade outwards from the fine resolution region toward the coarse resolution region. Resolutions differ by a factor of two between two adjacent VR regions. On a VR boundary, particle states are evenly exploded (moving from coarse cells to fine cells) or simply coalesced (moving from fine cells to coarse cells). Such a treatment exactly conserves local mass and momentum and gives continuous fluid density and velocity across VR boundaries.

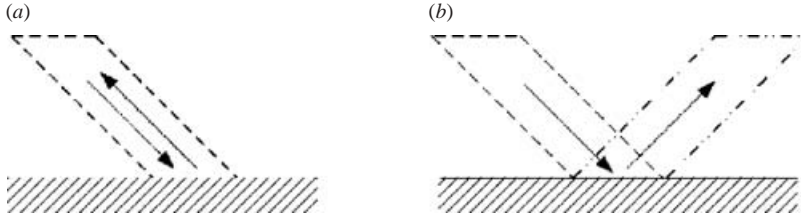


FIGURE 3. Implementation of boundary condition with (a) bounce back and (b) specular reflection in the LBM.

A refined VR scheme (based on additional linear interpolations) is also tested, and the difference in results in this specific study is negligible.

One of the advantages of LBM is its capability of dealing with complex geometries. A simple particle bounce back process on the solid boundary reverses all particle velocity directions such that the no-slip boundary condition is realized, while a particle specular reflection process reverses the normal velocity components and maintains the tangential velocity directions so that the free-slip boundary condition is satisfied (figure 3). Point-wise implementation of the bounce-back and the specular reflection scheme has been used successfully in lattice aligned cases. However, this scheme fails to provide accurate and smooth results on curved geometries (Chen & Doolen 1997). The effective numerical surface roughness caused by non-smooth boundary schemes can produce an undesirable influence on the evolution of the boundary layer. Although many modified bounce-back schemes with high-order interpolations have been proposed, sufficiently smooth results, such as surface pressure distribution, are difficult to achieve on a curved geometry (Filippova & Hanel 1998; Mei & Shyy 1998; Ginzburg & d'Humières 2003). Furthermore, higher-order pointwise interpolation schemes cannot ensure exact mass flux while maintaining the detailed balance among particle distributions (Chen 1998). A proper realization of boundary conditions has been shown to be crucial for incorporating turbulent boundary-layer physics for high-Reynolds-number flow simulations (Chen *et al.* 1998).

To overcome these shortcomings, an improved volumetric boundary scheme is applied in this study (Chen *et al.* 1998). In this scheme, either particle bounce back or specular reflection is conducted right on a discretized (facetized) surface comprised of a set of planar surface elements (facets). Each facet has a set of extruded parallelograms (parallelepiped in three dimensions) corresponding to the discrete directions (\mathbf{c}_i) with the volumes, $V_i^\alpha = |\mathbf{c}_i \cdot \mathbf{n}^\alpha| A^\alpha \Delta t$. Here, \mathbf{n} is a surface normal of the facet pointing towards the fluid domain side, and A^α is the surface area of the facet. The related geometry definitions are shown in figure 4 and the volumetric bounce-back procedure is described briefly as the following. First, the parallelogram associated with the negative i th direction of velocity \mathbf{c}_i collects particles which are going to hit the facet in one time step from its neighbour cells according to the overlapping areas (overlapping volumes in three dimensions). The particle directions are then reversed ($\mathbf{c}_i \rightarrow -\mathbf{c}_i$), and particles are evenly distributed back to the neighbour cells according to the same overlapping areas with the parallelogram. More details can be found in Chen *et al.* (1998).

Such a volumetric scheme allows for precise control for various hydrodynamic fluxes. In addition, owing to the existence of a detailed balance condition (Chen *et al.* 1998), it can be shown that it does not generate spurious currents, thus numerical

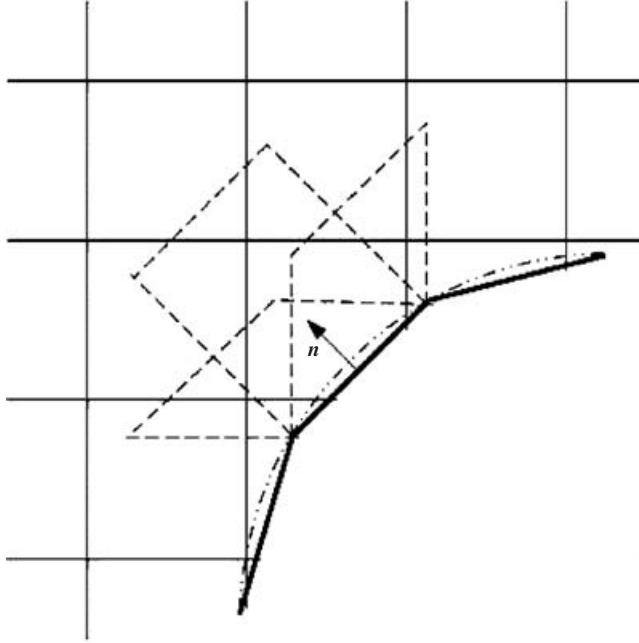


FIGURE 4. Geometry definitions for the volumetric boundary scheme in the current study. The dark-solid line segments are facets of the original surface (dash-dotted line), the dashed-line-bounded regions represent parallelograms.

surface noise is greatly reduced. Many benchmark studies have been done using this scheme and results are promising (Shock *et al.* 2002; Chen *et al.* 2003).

The original volumetric scheme is shown to be first-order accurate on a non-lattice aligned surface. To further improve this approach, a correction $\delta\Gamma_i^\alpha(\mathbf{x})$ according to local velocity gradient is added to the original, evenly bounced-back particles:

$$\left. \begin{aligned} \delta\Gamma_i^\alpha(\mathbf{x}) &= V_i^\alpha(\mathbf{x})\delta f_i^\alpha(y^\alpha(\mathbf{x}) - y_i^\alpha), \\ \delta f_i^\alpha &= \rho w_i \frac{\mathbf{c}_i \cdot \mathbf{F}^\alpha}{T}, \\ \mathbf{F}^\alpha &= \frac{\partial \mathbf{u}}{\partial y}, \end{aligned} \right\} \quad (2.9)$$

where $V_i^\alpha(\mathbf{x})$ is the parallelogram overlapping area in cell \mathbf{x} which is associated with state i from facet α (Chen *et al.* 1998), $y^\alpha(\mathbf{x})$ is the distance from \mathbf{x} to facet α and

$$y_i^\alpha = \frac{\sum_{\mathbf{x}} y^\alpha(\mathbf{x})V_i^\alpha(\mathbf{x})}{\sum_{\mathbf{x}} V_i^\alpha(\mathbf{x})} \quad (2.10)$$

is the weighted average distance of $y^\alpha(\mathbf{x})$ among all cells overlapping with a parallelogram of state i .

With the extra velocity-gradient-dependent term, the particle state distribution is now redistributed linearly in each parallelogram, as opposed to the original evenly distributed one. It is easy to show that $\sum_i (\text{equation (2.9)}) = 0$ and $\sum_i (c_i \cdot \text{equation$

(2.9)) = 0. Thus, the correction does not alter the original exact mass and momentum conservations.

3. LBM simulation case set-up

The hydrodynamics of the flow induced by an impulsively started cylinder with constant velocity $-U_o$ is equivalent to that of an impulsively started fluid flow with the same free-stream velocity U_o passing a static circular cylinder. For the convenience of simulations, we choose the latter case for study in this paper.

3.1. Case definition

When the Reynolds number is below a critical value ($Re_{critical} = 45 \sim 49$), the flow field around a cylinder is stable. The flow structures are primarily characterized by the formation of a symmetrical recirculation zone behind the cylinder containing a pair of counter-rotating stationary eddies with equal strengths and sizes. Even with an impulsive start, the flow is finally able to reach a steady state without any vortex shedding or symmetry breaking. On the other hand, when the Reynolds number is beyond the critical range, the flow structures start to lose symmetry and become unstable. Shedding vortices occur and a steady state cannot be reached. At moderate Reynolds numbers (e.g. $Re \approx 550$), the impulsively started flow field is also marked by the formation of small secondary vortices located downstream of the boundary-layer separation regions. These flow phenomena have been observed both in numerical computations (Loc 1980, hereinafter referred to as L1980; Smith & Stansby 1988, hereinafter referred to as SS1988; Chang & Chern 1991, hereinafter referred to as CC1991; Wang & Dalton 1991, hereinafter referred to as WD1991; Koumoutsakos & Leonard 1995, hereinafter referred to as KL1995; He & Doolen 1997, hereinafter referred to as HD1997; Ploumhans & Winckelmans 2000, hereinafter referred to as PW2000) and in experiments (Coutanceau & Bouard 1977*a, b*, hereinafter referred to as CB1977; Bouard & Coutanceau 1980, hereinafter referred to as BC1980).

In this study, we focus on two different and representative Reynolds numbers, $Re = 40$ and $Re = 550$. For simulations of $Re = 40$, the computations are run up to $T = 250$. This is not only to capture unsteady flow features ($T \leq 25$), but also to reach a final steady-state solution. For the case of $Re = 550$, simulations are run for a relatively short amount of time, $T \leq 7$, when the flow symmetry still holds in experiments (Bouard & Coutanceau 1980).

A sketch of these flow features is provided in figure 5. The wake length is defined as the length of the reattachment point, C , to the base suction point, B , on the cylinder surface. Points a and b give the location for the centre of the primary eddy. The separation angles for the primary eddies and secondary vortices are measured from the base suction point on the cylinder to the separation point S . Here, the separation point is defined as the position with zero wall shear stress: $\tau_{wall} = 0$. Such a definition is consistent with former studies (such as in Bar-Lev & Yang 1975; He & Doolen 1997).

3.2. Numerical set-ups

Theoretically, the flow domain is not confined. However, in numerical simulations fictitious computational boundaries are required. These are set at a distance sufficiently far away from the cylinder so that any outer boundary effect may be neglected. In the computational set-up, the external boundaries are placed to minimize the blockage effect as well as to keep the computational cost affordable.

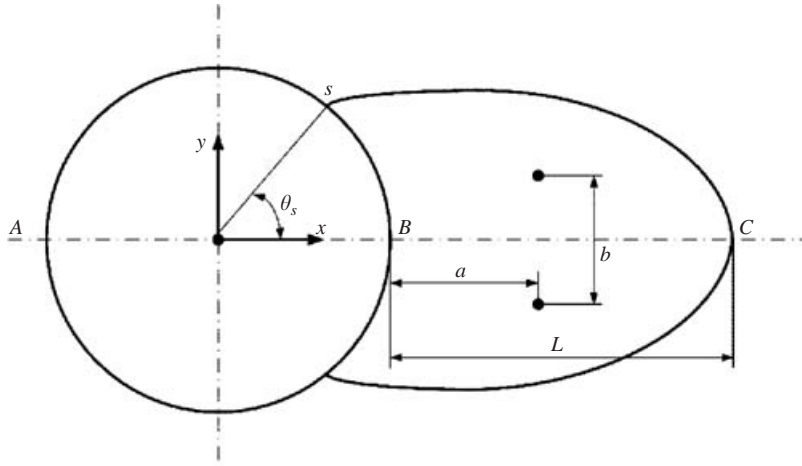


FIGURE 5. Geometrical parameters of the closed wake for flow past an impulsively started cylinder at low Reynolds numbers.

For the case of $Re = 40$, computational boundaries in the x - and y -directions are placed at 50 diameters away from the centre of the cylinder. This set-up is similar to that used by He & Doolen (1997). Further placement of the outer boundaries turns out to have little effect on simulation results. There are 80 finest cells across the cylinder and the total number of simulation cells is about 230 000.

The set-up of the $Re = 550$ case is slightly different from the case of $Re = 40$. The upstream boundary is 20 diameters away, and the downstream boundary is 40 diameters away from the centre of the cylinder. The vertical boundaries are 17 diameters away in each direction (figure 2) (this set-up is similar to that used by Persillon & Braza 1998 in the study of wake transition phenomena). The resolution across the cylinder is 160 finest cells, the total number of simulation cells is close to one million.

3.3. Boundary and initial conditions

On the cylinder surface, the boundary conditions are those of impermeability and no-slip, as discussed in the previous sections. On the inlet boundary, a uniform velocity profile $U_{inlet} = U_o \hat{x}$ is imposed. On the far-field outlet, a static pressure boundary condition with $P_{out} = constant$ is imposed. Although this is not absolutely physical for unsteady flows (it could generate low-level non-physical reflection waves at the boundary), it can still serve as a close enough approximation in the simulations. Since the outlet is quite far away from the cylinder, the pressure wave generated from the impulsive start travels a relatively long time before it is reflected back, thus its influence on flow dynamics near the cylinder at an early stage is negligible. In the perpendicular y -direction, a periodic boundary condition is used for simplicity.

In the specification of initial condition, an irrotational potential flow solution is imposed at $T = 0^+$ (at time $T = 0$ flow is still at rest according to the impulsive start definition) in most of the previous studies (Chang & Chern 1991; Koumoutsakos & Leonard 1995; He & Doolen 1997; Ploumhans & Winckelmans 2000). This solution is also used in the current study simply because of its popularity in the former numerical and theoretical works.

Strictly speaking, such a specification of the initial conditions is not an exact reflection of the onset of the impulsive start ($T = 0^+$). There exists no analytical solution for this type of problem. The instantaneous start-up process generates a very thin

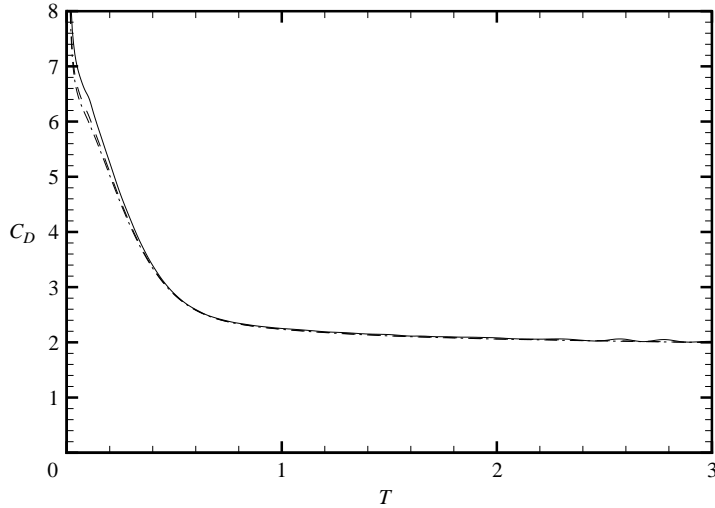


FIGURE 6. Convergence study for the flow past an impulsively started cylinder at $Re = 40$.
 —, $\beta = 40$; ---, $\beta = 80$; -·-, $\beta = 160$.

and strong vorticity sheet around the cylinder. Since the vorticity is concentrated only in a tiny region near the cylinder with a near-zero thickness in numerical analysis, a potential flow initial condition is a reasonable approximation (Chang & Chern 1991; Anderson & Reider 1996). Loc & Bouard (1985) argued that the initial flow is still in the Stokes regime and imposed a solution of the Navier–Stokes equations at very low Reynolds number ($Re = 5$) as the initial condition. Collins & Dennis (1973a) also adopted a boundary-layer solution as the initial condition in their theoretical formulations. In experiment, Bouard & Coutanceau (1980) accelerated the cylinder in a very short time, $T \leq 0.02$, to approximate this impulsive start. The LBM in the current study is a weakly compressible solver. Any discontinuity introduced by initial conditions will be relaxed and propagated at a finite speed of sound. In this sense, this behaviour may better reveal the initial flow development in reality.

4. Results and discussion

Convergence studies are first performed to obtain a grid-independent solution. Here, we define a grid resolution parameter $\beta = D/\delta h$, where D is the diameter of cylinder and δh is the finest grid (cell) size. For $Re = 40$, three different grid resolutions, $\beta = 40, 80$ and 160 are used for the study, while for $Re = 550$, resolutions with $\beta = 160$ and 320 are used. Both simulations are performed at a low Mach number ($M = 0.1$). Figures 6 and 7 show the drag history. The results indicate that the resolutions of 80 and 160 are sufficient for $Re = 40$ and $Re = 550$ to obtain convergent results, respectively. Certainly, further refinements might be able to capture more detailed features of the unsteadiness right after the impulsive start ($T \leq 0.5$). Considering the computational cost, these two resolutions with $M = 0.1$ are used as the defaults for the following studies unless mentioned explicitly.

On an IBM 44P270 machine with 4 CPUs running at 375 MHz, the memory and CPU time requirements for the $Re = 40$ case are 41.3 Megabytes and 9602.32 s (wallclock) for a total of 17 321 time steps (corresponding to $T = 25$). The simulations

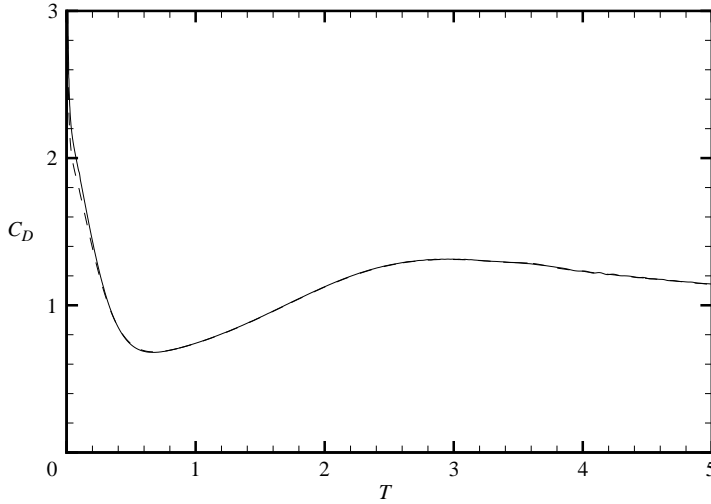


FIGURE 7. Convergence study for the flow past an impulsively started cylinder at $Re = 550$. —, $\beta = 160$; ---, $\beta = 320$.

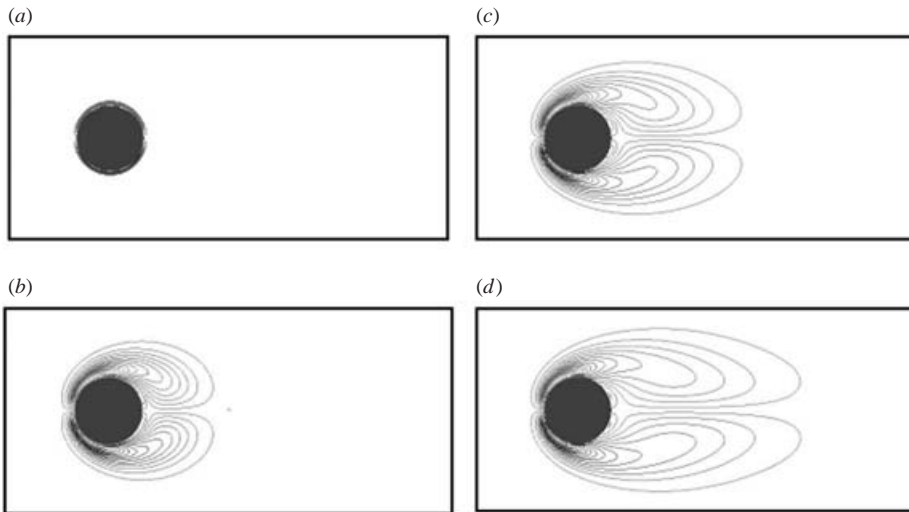


FIGURE 8. Vorticity iso-contours of an impulsively started circular cylinder at $Re = 40$. (a) $T = 0^+$, (b) $T = 2.5$, (c) $T = 5.0$, (d) $T = 7.5$.

for $Re = 550$ require 58.1 Megabytes memory and 7745.48 s (wallclock) simulation time to reach 9699 time steps (corresponding to $T = 7$).

4.1. Numerical results for flows at $Re = 40$

At small to moderate Reynolds numbers, say $Re = 40$, the flow reaches a steady state after the impulsive start. No vortex shedding occurs. The key flow characteristics include the flow separation angle, wake recirculation length and wake centreline velocity distributions. In order to ensure the system has reached a steady state, we continue the simulation for a sufficiently long time.

The temporal evolution of the vorticity field from our simulation (referred to as present work hereinafter) is shown in figure 8. At time $T = 0^+$, a thin layer of vorticity

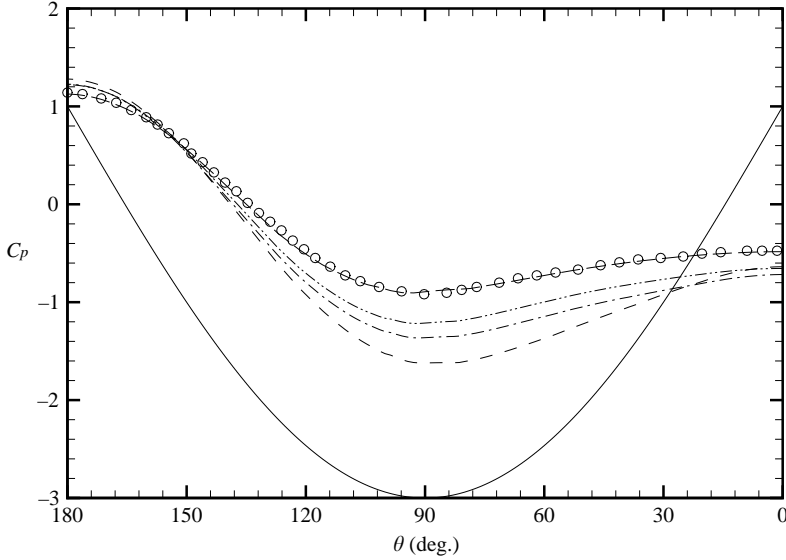


FIGURE 9. Surface pressure coefficient distribution of an impulsively started circular cylinder at $Re = 40$. —, $T = 0$; ---, $T = 2.5$; -·-, $T = 5.0$; ···, $T = 7.5$; - - - , $T = 250$; ○, LBM-HD1997.

is generated on the cylinder surface owing to the impulsive start. This vorticity quickly diffuses and propagates downstream owing to the strong convection of the mean flow. Meanwhile, a very thin boundary layer forms on the cylinder surface. The flow on the downstream side near the cylinder surface experiences a significant friction loss and does not have enough kinetic energy to move further along the surface with an adverse pressure gradient. Consequently, the flow separates from the cylinder surface, and secondary counter-rotating vortices (with respect to the primary ones) appear at the rear of the cylinder. These secondary vortices are confined by the primary vortices and are clearly visible at time $T = 2.5$. The vortices tend to smooth out the pressure gradient on the rear cylinder surface (figure 9) and yield a corresponding decrease in the drag force acting on the cylinder. Finally, a symmetric wake reaches a steady state (figure 10) with a parabolic-like shape which is Reynolds-number dependent. The predicted wake pattern matches well with the experimental observation (Coutanceau & Bouard 1977*a, b*).

Also notice that in the surface pressure distribution (figure 9), our simulation predicts a steady-state solution ($T = 250$) of pressure coefficient $C_p = 1.15$ at the front stagnation point. This might be due to the Barker effect as discussed in Schlichting & Gersten (2000) for plane stagnation-point flow and the result is consistent with other numerical results of He & Doolen (1997) ($C_p = 1.13$) and Fornberg (1980) ($C_p = 1.14$). For the pressure distribution on the cylinder surface, the present work (figure 9) shows a good agreement of the steady-state surface-pressure distribution with the previous LBM work of He & Doolen (1997).

Table 1 gives a quantitative summary of some geometrical flow properties at steady state compared with experiment and other numerical methods. Table 2 gives some dynamic flow characteristics, such as the drag coefficient, pressure coefficient at the front/rear stagnation points. These comparisons demonstrate the accuracy of the present LBM approach.

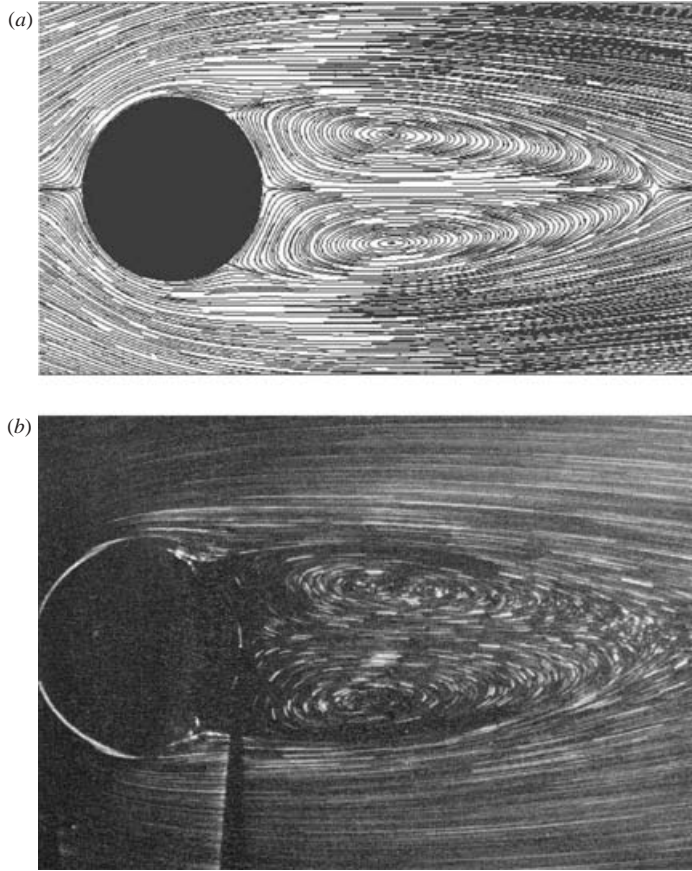


FIGURE 10. Comparison of (a) steady-state streamline pattern of LBM-present work ($Re = 40$) with (b) experimental streakline pattern (CB1977-exp, $Re = 40.3$, diameter ratio $D/L = 0.07$, where L is the characteristic length associated with the experimental flow volume).

Authors	θ_s	L/R	a/D	$b/2D$
CD1973 (Collins & Dennis 1973b)	53.6	4.3	–	–
CB1977	53.5	4.26	1.52	1.19
F1980 (Fornberg 1980)	–	4.48	–	–
KL1995	53.03	–	–	–
HD1997	52.84	4.49	–	–
MS1998 (Mei & Shyy 1998)	50.12	4.38	–	–
GSW2000 (Guo <i>et al.</i> 2000)	53.13	4.40	–	–
Present	53.13	4.34	1.50	1.16

TABLE 1. Comparison of geometrical parameters with previous studies for impulsively started flow at $Re = 40$.

For impulsively started flows, it is difficult to capture time evolution behaviour even for relatively low Reynolds numbers. In figures 11–14, we present the time evolution of various computed flow quantities. Figure 11 shows the x -component velocity distribution along the symmetry axis behind the cylinder at four different times. It is seen that the results match the experimental measurements well, especially

Authors	C_D	$C_p(\pi)$	$C_p(0)$
CD1973	1.56	—	—
CB1977	—	—	—
F1980	1.498	1.14	-0.46
KL1995	1.628	—	—
HD1997	1.499	1.133	-0.487
present	1.55	1.15	-0.48

TABLE 2. Comparison of dynamic parameters with previous studies for impulsively started flow at $Re = 40$.

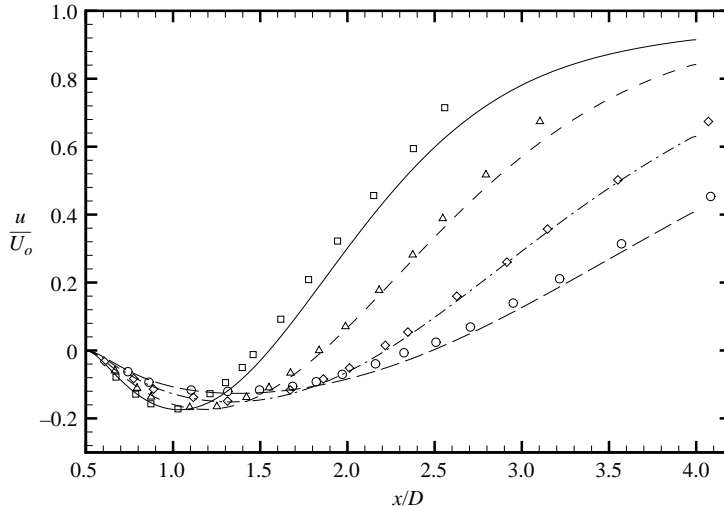


FIGURE 11. Comparison of x -velocity distribution on the flow axis behind an impulsively started cylinder at $Re = 40$. \square , CB1977-exp, $T = 5.4$; —, LBM-present work, $T = 5.5$; \triangle , CB1977-exp, $T = 7.4$; ---, LBM-present work, $T = 7.5$; \diamond , CB1977-exp, $T = 10.6$; ---, LBM-present work, $T = 10.5$; \circ , CB1977-exp, $T = 14$; ---, LBM-present work, $T = 14$.

in the enclosed wake region. However, our predicted axial x -velocity deviates slightly from those of experiment after the reattachment. We believe that this difference is mainly because the present numerical simulation volume (relative to the cylinder size) is eight times larger than that used in experiment (diameter ratio $D/L = 0.07$). Consequently, the blockage effect may be stronger in experiment. This may reduce the relative inertial effect on the standing eddies which thus become less developed, as remarked by Coutanceau & Bouard (1977b). Also notice that the corresponding data is taken at slightly different times compared with experiment, for instance $T = 7.5$ (present work) and $T = 7.4$ (experiment). However, this slight time difference is negligible compared to the other effects mentioned. Another potential cause of discrepancy is the three-dimensionality. On the other hand, it is argued that such an effect should be ignorable since, in the early stage, the flow is predominantly laminar and two-dimensional (Chang & Chern 1991).

Figure 12 shows the time evolution of the separation point compared with the vortex method (Koumoutsakos & Leonard 1995), the previous LBM (He & Doolen 1997) and the experiment (Coutanceau & Bouard 1977b). All numerical results shortly after the impulsive start are close to each other, but differ slightly from experiment.

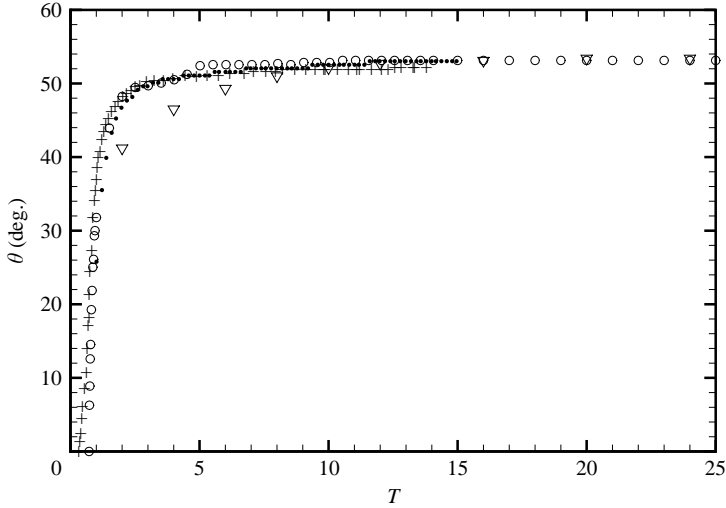


FIGURE 12. Time evolution of the separation angle at $Re=40$. \circ , LBM-present work; $+$, LBM-HD1997; \bullet , KL1995; ∇ , CB1977-exp.

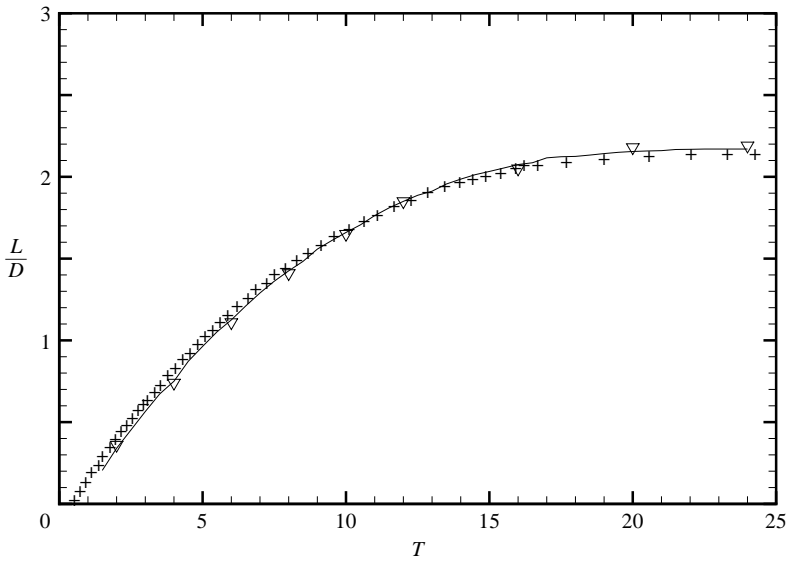


FIGURE 13. Time evolution of the enclosed wake length at $Re=40$. ∇ , CB1977-exp; —, LBM-present work; $+$, LBM-HD1997.

At ($T \leq 1$), our result shows that the separation occurs at $T=0.72$ while He & Doolen (1997) gave a value of approximately 0.5. Our simulation also predicts a slightly faster development of separation (with a steeper slope). At time $T \in [2, 8]$, all numerical results deviate from the experiment. This is mainly because the separation observed in experiment actually corresponds to a sudden large increase of boundary-layer thickness along the cylinder surface (similar to the singularity definition used in Schlichting & Gersten 2000). For unsteady flows, such a definition might not be equivalent to the one given by the zero wall shear stress definition used in present and other numerical/theoretical studies. In our present result there exists a curvature

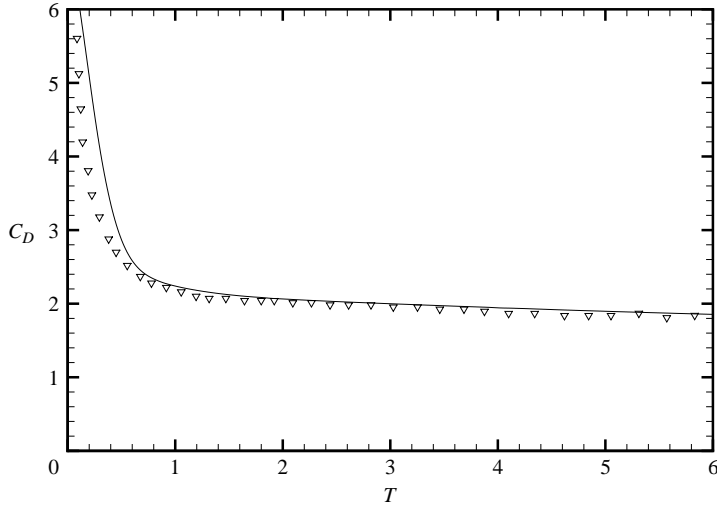


FIGURE 14. Comparison of total drag history for an impulsively started cylinder at $Re = 40$. —, LBM; ∇ ; KL1995.

change between $T = 2$ and $T = 5$. After sufficient time ($T \geq 8$), our result once again agrees quite well with the experimental data.

Figure 13 show the numerical results of the enclosed wake development. The evolutions of wake length agree well with experimental values and He & Doolen's (1997) results. It is also worth mentioning that the experimental data shown in the figure includes modifications to the actual values (diameter ratio $D/L = 0.025$) to correct for its own blockage effect (Coutanceau & Bouard 1977b).

The time evolution of total drag is shown in figure 14. This is compared with the available results from the vortex method (Koumoutsakos & Leonard 1995). For $T \geq 1$, the results are in good agreement, showing a continuous decay until reaching a steady state. At the onset of the flow, the vortex method gives a much more rapid decrease of the drag (square root singularity). Present work shows a slower decay mainly because of the LBM finite-compressibility effect. This will be further commented on in the discussion section.

4.2. Numerical results for flows at $Re = 550$

When the Reynolds number is high ($Re = 550$), the flow pattern becomes more complex and a number of highly nonlinear flow phenomena occur (figures 15 and 16). The secondary vortices appear within $T = 1$. Compared with low-Reynolds-number flow ($Re = 40$), the flow separation is earlier and the wake recirculation is stronger. As a result, the secondary vortices are bigger and stronger at $T = 3$ and $T = 5$. Small-scale flow structures also continue to grow in time, but remain confined by the primary vortices up to $T = 5$. These unsteady, small vortices further impact the evolution of the primary vortices. These properties are also reflected in the surface pressure distributions where the vortical structures induce large spatial fluctuations in the pressure coefficient on the rear cylinder surface (figure 17). It is noted that the pressure gradient changes sign twice on the rear surface of the cylinder at time $T = 3$ and $T = 5$, which implies a generation of local secondary flows. In our simulation, the secondary vortex starts at time $T = 2.635$ and is located at about 42.67° from the symmetry axis. This result nearly agrees with the result of the vortex method

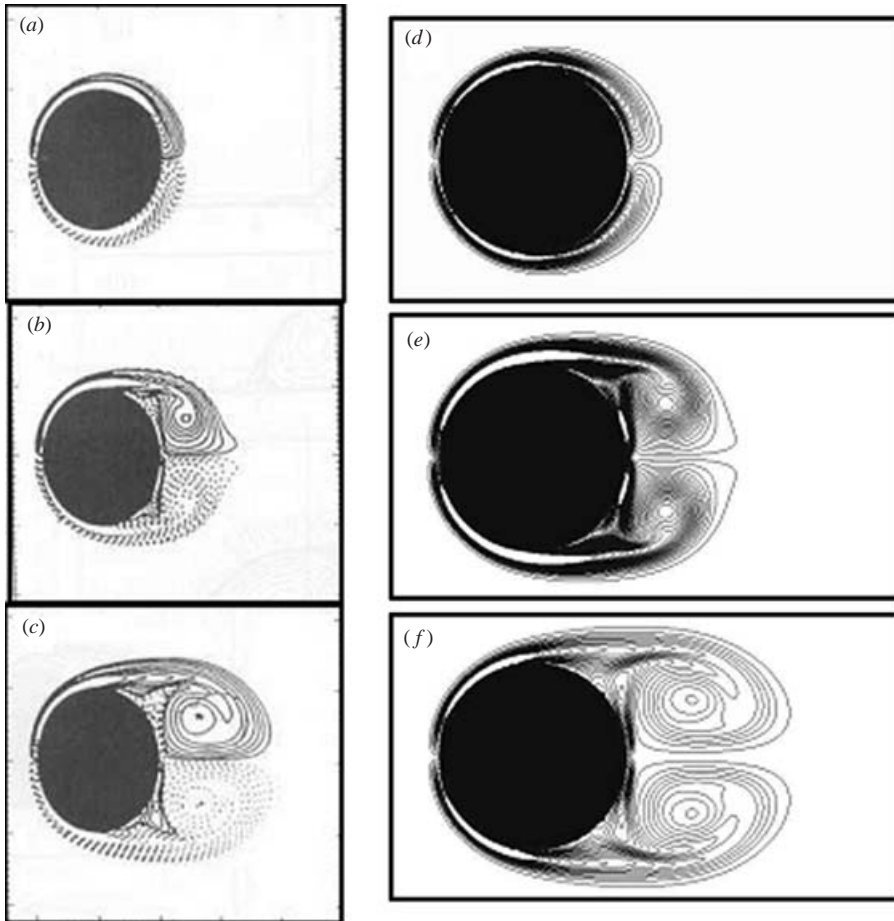


FIGURE 15. Vorticity iso-contours at $Re=550$. (a) KL1995, $T=1$, (b) KL1995, $T=3$, (c) KL1995, $T=5$, (d) LBM-present work, $T=1$, (e) LBM-present work, $T=3$, (f) LBM-present work, $T=5$.

($T=2.85$) of Loc (1980) and result of He & Doolen (1997) ($T=2.75$). Again, like the case of $Re=40$, the vorticity field and streamline field are in good agreement with other numerical results and experimental observations (figures 15 and 16).

Figures 18 and 19 show the velocity evolution along the symmetry axes behind the cylinder. The only other available numerical result is from Loc (1980). Since he used the steady-state viscous solution of very low Reynolds number ($Re=5$) as the initial condition (which imposed a vorticity field throughout the flow initially), the flow velocity in the wake region seems underestimated compared with our present results.

The results of the early time evolution of the enclosed wake are shown in figure 20. This wake quantity is close to the experimental data and He & Doolen's (1997) solution.

The measurement of the locations of zero shear stress in time represents a more detailed study. Figure 21 clearly shows the time evolution of the separation/reattachment points related to the primary and secondary vortices. Compared with Koumoutsakos & Leonard's (1995) result, we have a $1 \sim 3$ degree difference in the prediction of these points. In the case with $\beta=160$, the first separation occurs at time

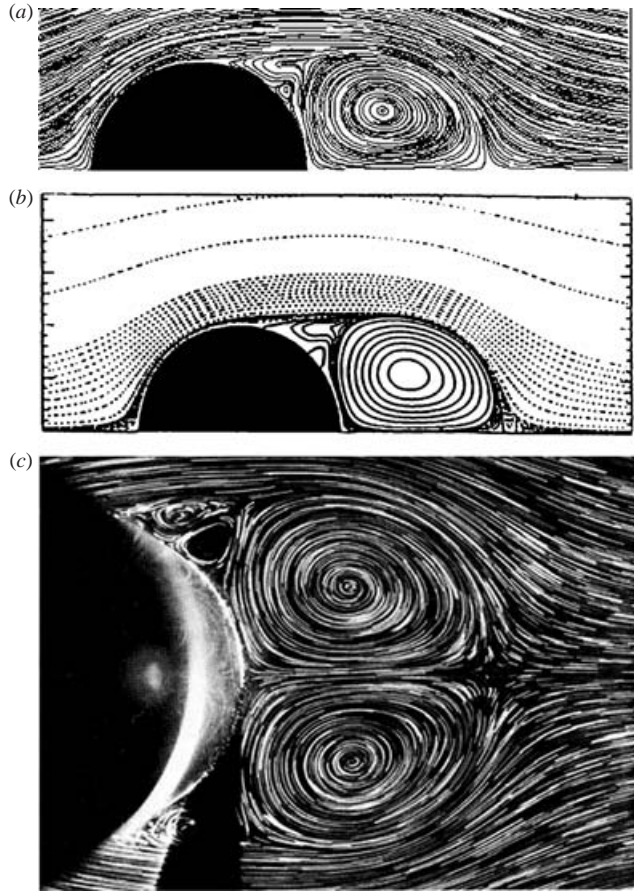


FIGURE 16. Stream contours at $Re = 550$, $T = 5$. (a) LBM-present work, (b) KL1995, (c) BC1980-exp.

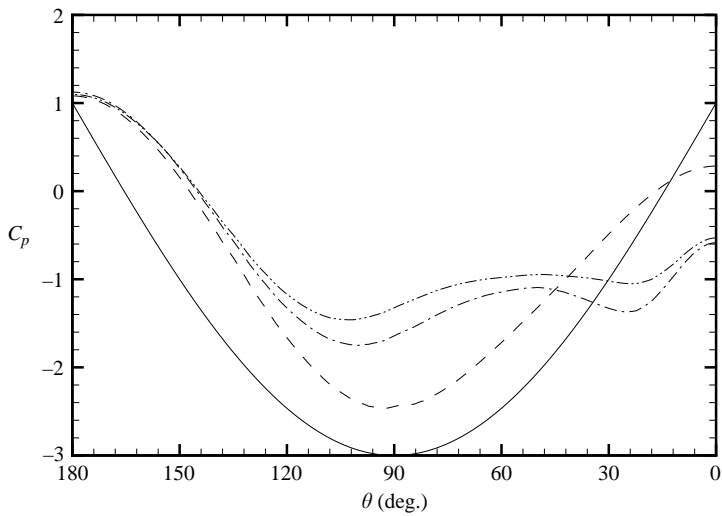


FIGURE 17. Surface pressure distribution for flow past an impulsively started cylinder at $Re = 550$. —, $T = 0$; ---, $T = 1$; -·-, $T = 3$; ·-·-, $T = 5$.

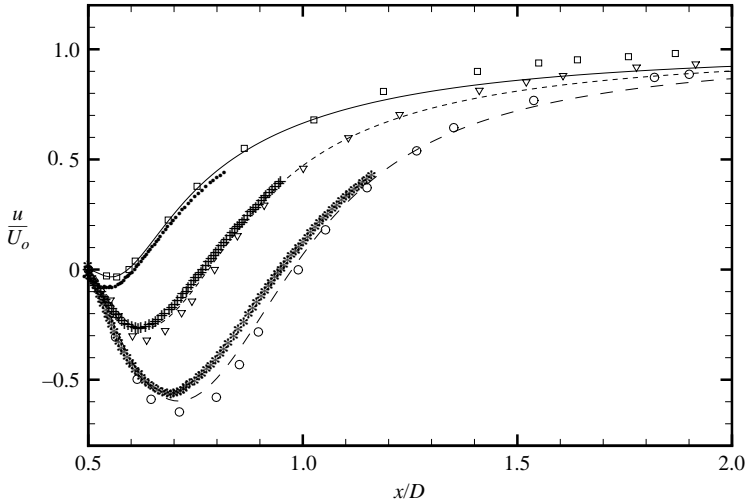


FIGURE 18. Comparison of x -velocity distribution on the flow axis behind an impulsively started cylinder at $Re = 550$. \square , BC1980-exp, $T = 1$; \blacksquare , TL1980, $T = 1$; —, LBM-present work, $T = 1$; ∇ , BC1980-exp, $T = 2$; $+$, TL1980, $T = 2$; ---, LBM-present work, $T = 2$; \circ , BC1980-exp, $T = 3$; \star , TL1980, $T = 3$; -.-, LBM-present work, $T = 3$.

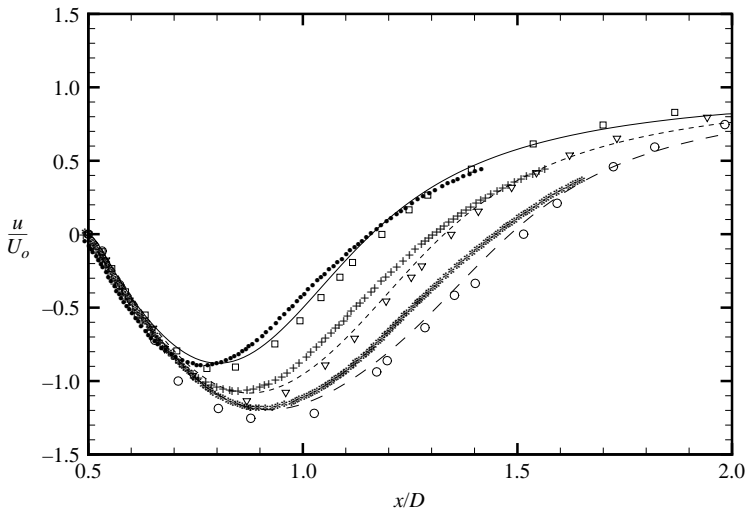


FIGURE 19. Comparison of x -velocity distribution on the flow axis behind an impulsively started cylinder at $Re = 550$. \square , BC1980-exp, $T = 4$; \blacksquare , TL1980, $T = 4$; —, LBM-present work, $T = 4$; ∇ , BC1980-exp, $T = 5$; $+$, TL1980, $T = 5$; ---, LBM-present work, $T = 5$; \circ , BC1980-exp, $T = 6$; \star , TL1980, $T = 6$; -.-, LBM-present work, $T = 6$.

$T_{s1} = 0.44$, while Koumoutsakos & Leonard (1995) showed $T_{s1} \approx 0.20$. The analytic solution by Bar-Lev & Yang (1975) gives $T_{s1} = 0.3621$. A further study shows that with a reduced compressibility (smaller Mach number) and increased resolution, the LBM predicts earlier separation time for the first separation. This indicates that compressibility might be a reason for the prediction of the delayed onset of separations. The results with respect to the first separation and the onset of the secondary phenomena (T_{s2}) are included in table 3, along with available results from other works.

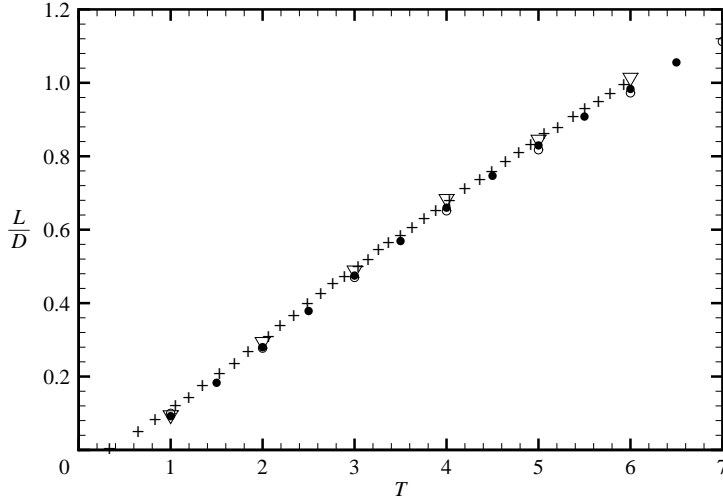


FIGURE 20. Comparison of the time evolution of the wake length at $Re = 550$. ●, LBM-present work; ▽, BC1980-exp; +, LBM-HD1997.

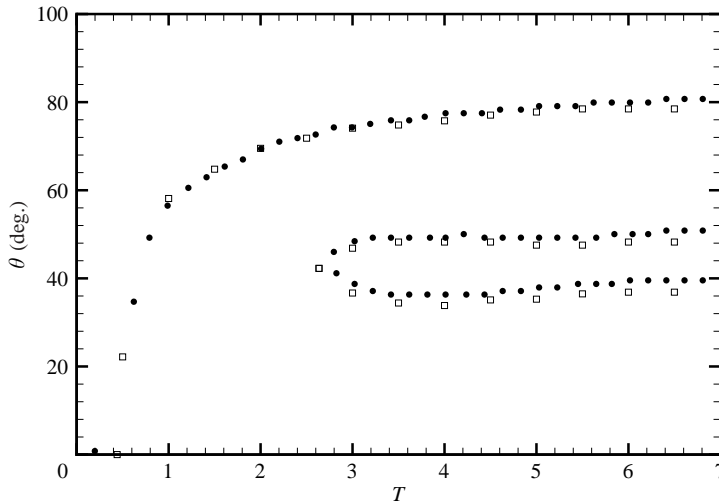


FIGURE 21. Time evolution of the separation/reattachment point on cylinder surface at $Re = 550$. ●, KL1995; □, LBM-present work.

The time evolution of the first separation point right after the impulsive start is shown in figure 22 with comparison to the analytic solution from Bar-Lev & Yang (1975). We predict a different result from the analytic one, and with a refined grid or reduced compressibility, a slightly improved separation is predicted in the early flow development ($T < 0.6$). However, both the high-resolution results and the Mach number study solutions converge for $T \geq 0.6$. At the corresponding time range, Koumoutsakos & Leonard (1995) showed a result with a substantially slower separation than in the present study. This implies that the difference between numerical results (both vortex methods and LBM) and Bar-Lev & Yang's (1975) theoretical solution might be due to other reasons, this requires further investigation.

	Relaxation time			Separation angle
	T_{peak}	T_{s1}	T_{s2}	at time T_{s2} θ_{s2}
$M = 0.10, \beta = 160$	0.099	0.440	2.635	42.67
$M = 0.15, \beta = 160$	0.144	0.449	2.614	42.46
$M = 0.20, \beta = 160$	0.189	0.462	2.588	42.44
$M = 0.10, \beta = 320$	0.097	0.415	2.610	41.93
$M = 0.15, \beta = 320$	0.142	0.423	2.591	42.46
$M = 0.20, \beta = 320$	0.187	0.437	2.564	42.47
BY1975(theory) (Bar-Lev & Yang 1975)	—	0.362	—	—
L1980	—	—	2.85	—
KL1995	—	≈ 0.20	≤ 3	—
HD1997	—	—	2.75	—

TABLE 3. Comparison of separation point with previous studies for impulsively started flow at $Re = 550$.

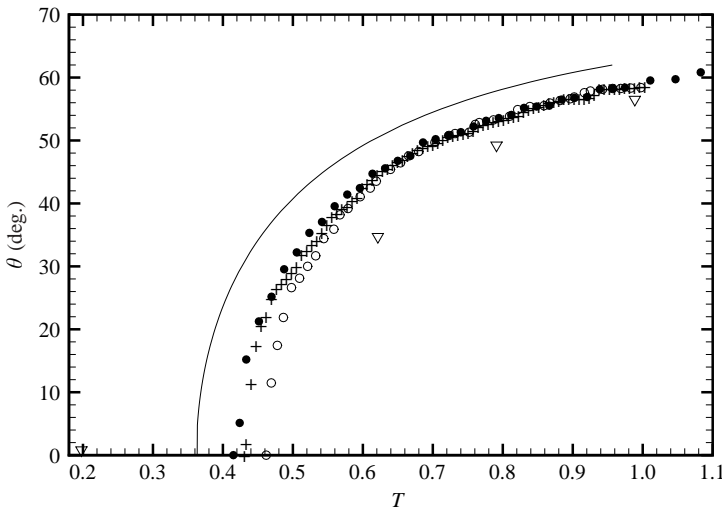


FIGURE 22. Time evolution of the separation point on cylinder surface at $Re = 550$ for $T \leq 1$. —, BY1975; ∇ ; KL1995, \circ , LBM with $M = 0.2, \beta = 160$; +, LBM with $M = 0.1, \beta = 160$; \bullet , LBM with $M = 0.1, \beta = 320$.

The comparison of the drag history in figure 23 shows good agreement with the vortex methods (Koumoutsakos & Leonard 1995; Ploumhans & Winckelmans 2000) for $T > 1$. However, when $T < 1$, our solution shows a relatively slower decrease in drag during the initial stage, while other results predict a square root singularity drop of the drag in time. This does not obey the asymptotic analysis given by Bar-Lev & Yang (1975). As shown below, we believe that this is again due to the finite compressibility effect in the LBM.

4.3. Discussion: compressibility effects during the initial stage

In general, our LBM approach gives accurate numerical results for the impulsively started flow field around a cylinder at relatively large time ($T \geq 1$). For short time immediately after the impulsive start, some results such as drag history are slightly

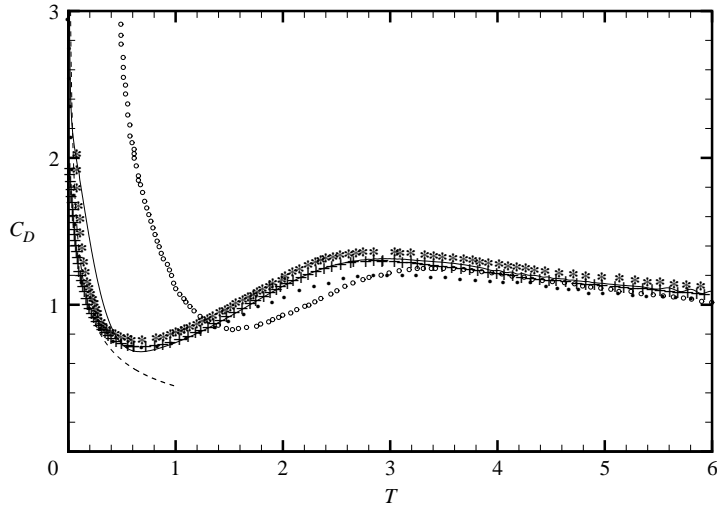


FIGURE 23. Total drag history comparison at $Re = 550$. ■, CC1991; +, KL1995; *, PW2000; ○, L1980; —, LBM-present work; ---, BY1975.

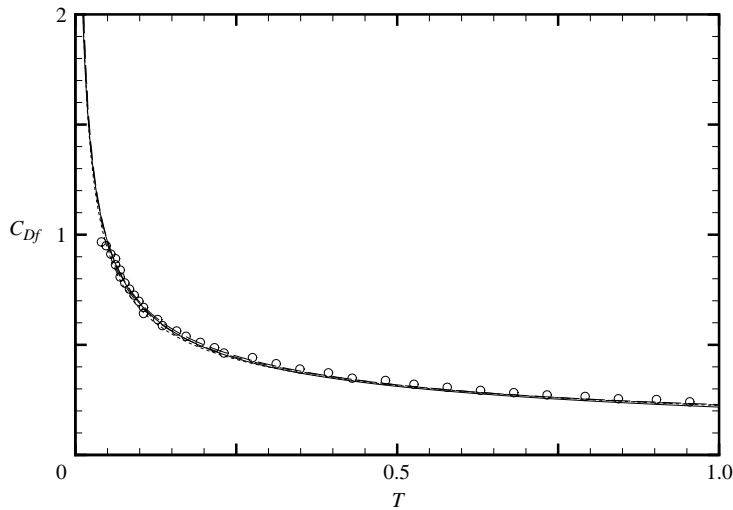


FIGURE 24. Friction drag history at $Re = 550$ for $T \leq 1$. ---, $M = 0.1$, $\beta = 160$; - · -, $M = 0.15$, $\beta = 160$; · · ·, $M = 0.2$, $\beta = 160$; - - -, $M = 0.1$, $\beta = 320$; ○, KL1995; —, BY1975.

different from other numerical and analytic solutions. A close look at the history of each drag component has provided some insights to its origin.

As is seen in figures 24, 25 and 26, both the vortex method and analytic solution predict a square root singularity in both the friction drag and pressure drag evolutions at the initial stage when $Re = 550$. These drag components make about the same contribution to the total drag when $T \leq 1$. Later the convection becomes stronger, and the pressure drag dominates the total force. The variation of pressure drag corresponds to the boundary-layer separation and the formation of the secondary flows. The friction drag retains a steadily decreasing trend until it reaches a steady value (figure 26).

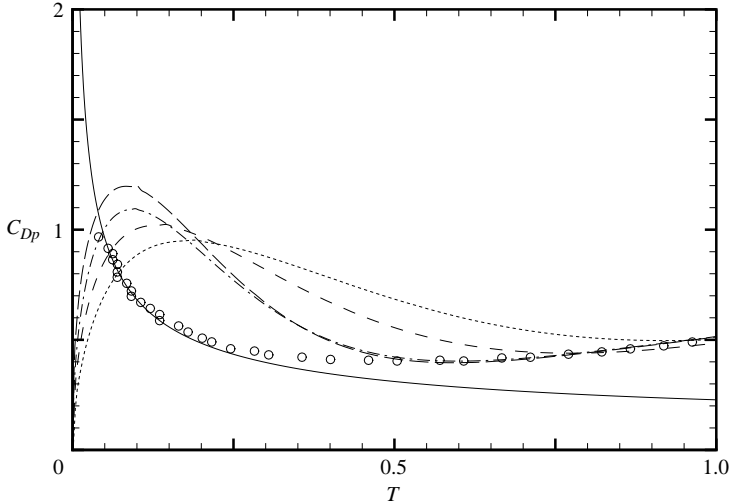


FIGURE 25. Pressure drag history at $Re = 550$ for $T \leq 1$. ---, $M = 0.1$, $\beta = 160$; - · -, $M = 0.15$, $\beta = 160$; · · · ·, $M = 0.2$, $\beta = 160$; \circ , KL1995; —, BY1975.

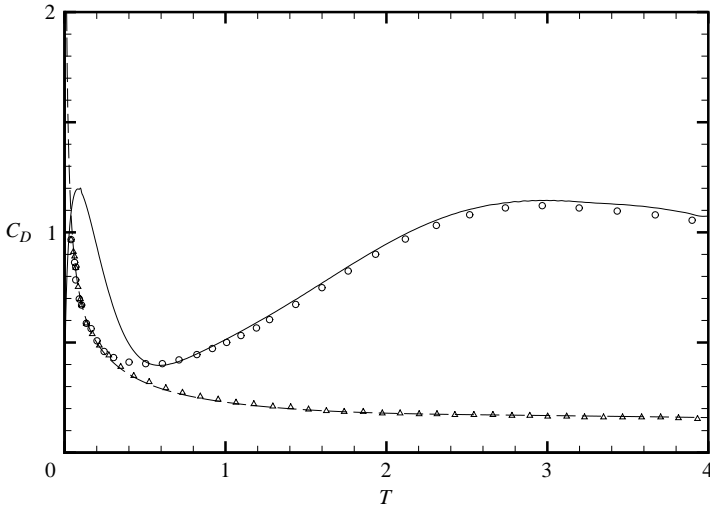


FIGURE 26. Friction drag and pressure drag history comparison at $Re = 550$. \circ , pressure drag of KL1995; Δ , friction drag of KL1995; —, pressure drag of LBM-present work, - · · -, friction drag of LBM-present work.

From our nearly incompressible LBM approach, a similar trend is predicted for the development of the friction drag with a square root singularity (figures 24 and 26). However, the pressure drag history (figures 25 and 26) shows quite a different behaviour. Initially, the pressure drag starts from zero (that is consistent with the potential flow initial condition used) and contributes little to the total drag. It then increases rapidly for a very short yet finite time (T_{peak}), before reaching its maximum. After that, it decreases quickly and converges to the results from other numerical solutions.

This substantial difference is because of the intrinsic compressible nature in LBM. For a purely incompressible flow, a thin and strong vortex layer around the surface of the cylinder occurs at $T = 0^+$ owing to the impulsive start. It has been shown

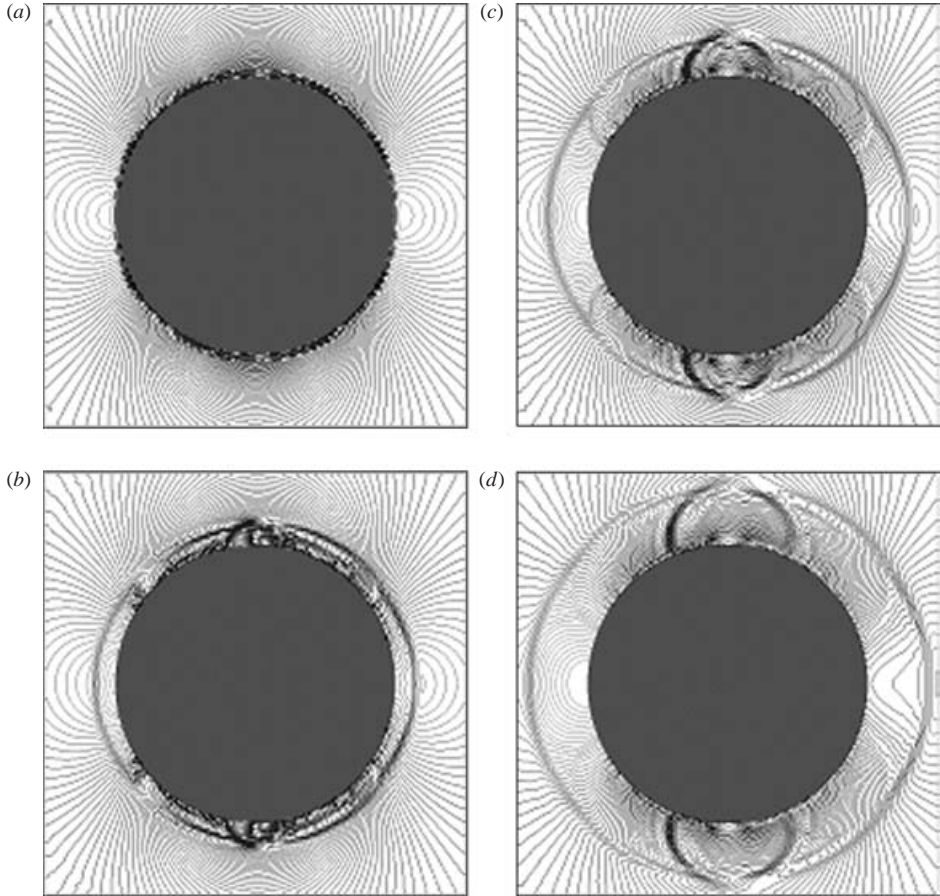


FIGURE 27. Pressure (density) field variation immediately after the impulsive start at $Re = 550$: (a) $T = 0$, (b) $T = 0.015$, (c) $T = 0.030$, (d) $T = 0.045$.

theoretically that this vortex layer decays at a rate inversely proportional to the square root of time at a very early stage ($T \leq 1$). This is directly responsible for the evolution of the friction force. Meanwhile, owing to incompressibility, the pressure field's response to the vortex is instantaneous. Hence, the pressure drag is expected to evolve in the same manner. Unlike the incompressible Navier–Stokes solvers, the LBM is a weakly compressible solver with an equation of state of an ideal gas. Any pressure fluctuation propagates at a finite speed of sound, $C_s = \sqrt{\gamma RT}$. This indicates a finite relaxation time, T_{peak} , to allow the pressure drag to reach its maximum after the impulsive start. This process can be further explained as the following. Right after the impulsive start, the flow on the cylinder surface will immediately be decelerated to zero velocity from the initial potential flow owing to no-slip. This corresponds to an infinite shear stress along the cylinder surface. The infinite shear stress tends to squash the flow in the streamwise direction while it generates a compensating expansion in the surface normal direction. The rapid stretching of fluid leads to the creation of a large pressure gradient in the boundary layer. This discontinuity propagates away from the cylinder at a finite speed of sound (figure 27) (note an incompressible flow is equivalent to having an infinite sound speed). However, this compressible process only lasts for a short time (T_{peak}), after which the usual viscous hydrodynamics take over.

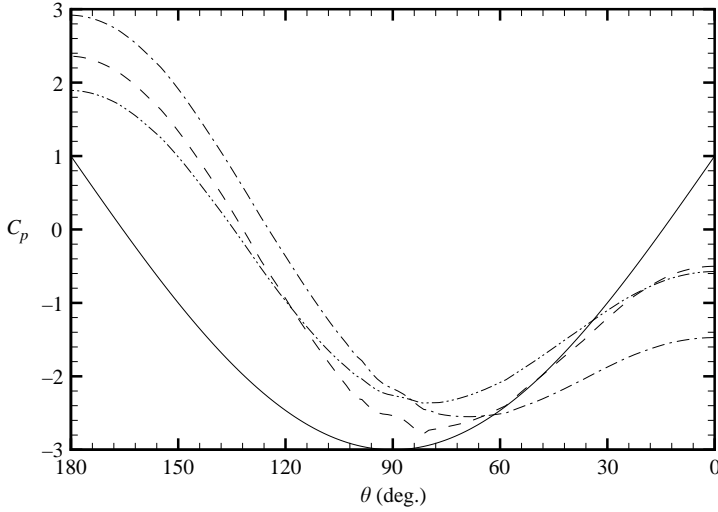


FIGURE 28. Surface pressure distribution for an impulsively started cylinder at $Re = 40$, $T < 1$. —, $T = 0$; ---, $T = 0.025$; -·-, $T = 0.1$; ···, $T = 0.4$.

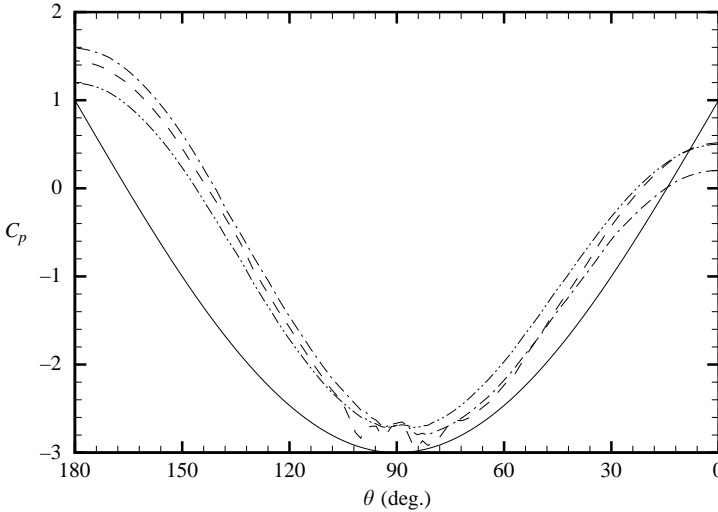


FIGURE 29. Surface pressure distribution for an impulsively started cylinder at $Re = 550$, $T < 1$. —, $T = 0$; ---, $T = 0.025$; -·-, $T = 0.1$; ···, $T = 0.4$.

The pressure drag then starts to decay at a rate close to that of the incompressible flow (figures 28 and 29). Thus, the monotonic decrease in pressure drag at a speed inversely proportional to the square root of time right after the impulsive start is a direct result of the incompressible assumption.

To confirm that the above phenomenon is closely related to the compressibility in LBM, a number of simulations at various Mach number values were performed. These are shown in figures 24 and 25. Indeed, convergence to incompressible solutions is observed as the Mach number is decreased. On the other hand, an increase in resolution only yields a rather marginal improvement. This suggests the numerical accuracy is not the cause of the discrepancy.

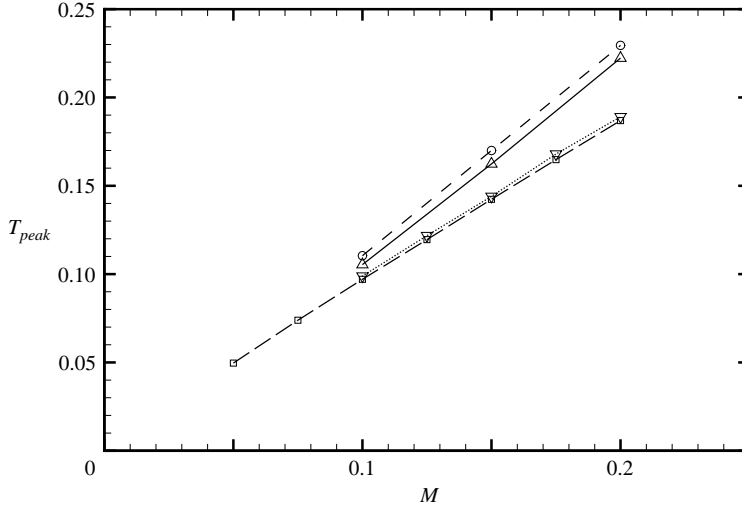


FIGURE 30. Relation between relaxation time and Mach number. --○--, $Re = 40$, $\beta = 160$; —△—, $Re = 40$, $\beta = 80$; ···▽···, $Re = 550$, $\beta = 160$; - -□ - -, $Re = 550$, $\beta = 320$.

Furthermore, we plot the relation between the relaxation time T_{peak} , and Mach number in figure 30. It clearly shows a linear dependence. This also confirms that T_{peak} would approach zero when Mach number reaches zero.

5. Conclusion

In this paper, we present a systematic study of flow past an impulsively started circular cylinder at both low and moderate Reynolds numbers. Using the extended weakly compressible LBM approach with a volumetric boundary treatment, the results compared well to well-established data obtained from theory, experiments, and other numerical methods. The differences of flow solutions in the initial stages are due to compressibility effects (at low Mach numbers) in LBM simulations. With additional computational resources, we plan to carry out simulations in the future on flows around an impulsively started cylinder at moderate to high Reynolds numbers in order to further verify our LBM approach.

It is worth mentioning that the Navier–Stokes equations are built upon a series of well-known assumptions for a Newtonian fluid (Schlichting & Gersten 2000). In addition, the no-slip wall boundary condition is also an approximation for flows near equilibrium (Gad-el-Hak 1999; Schlichting & Gersten 2000). On the other hand, LBM is kinetic theory based, thus it automatically contains some higher-order physics (Gad-el-Hak 1999; Chen *et al.* 2003), albeit this introduces entirely different types of issues associated with the discrete nature of the lattice models. In direct relevance to the main topic of paper, we suspect that the relatively robust behaviour in our impulsively started flow simulations may potentially be due to the more kinetic theory based boundary conditions. These will be the subject of extensive future investigations.

We wish to thank I. Staroselsky, S. Kandasamy, V. Yakhot for their valuable communications and comments, Y.L. would also like to acknowledge the useful suggestions from Dr T. Shih and Dr Z.J. Wang on the discussion of $C_p > 1$ at the front stagnation point.

REFERENCES

- ANDERSON, C. & REIDER, M. 1996 A high order explicit method for the computation of flow about a circular cylinder. *J. Comput. Phys.* **125**, 207–224.
- BAR-LEV, M. & YANG, H. 1975 Initial flow field over an impulsively started circular cylinder. *J. Fluid Mech.* **72**, 625–647.
- BEALE, J. T. & MAJDA, A. 1982a Vortex methods. I: Convergence in three dimensions. *Math. Comput.* **39**, 1–27.
- BEALE, J. T. & MAJDA, A. 1982b Vortex methods. II: High order accuracy in two and three dimensions. *Math. Comput.* **39**, 29–52.
- BHATNAGAR, P., GROSS, E. & KROOK, M. 1954 A model for collision processes in gases. I. small amplitude processes in charged and neutral one-component system. *Phys. Rev.* **94**, 511–525.
- BOUARD, R. & COUTANCEAU, M. 1980 The early stage of development of the wake behind an impulsively started cylinder for $40 < Re < 10^4$. *J. Fluid Mech.* **101**, 583–607.
- CHANG, C. & CHERN, R. 1991 A numerical study of flow around an impulsively started circular cylinder by a deterministic vortex method. *J. Fluid Mech.* **233**, 243–263.
- CHEN, H. 1998 Volumetric formulation of the lattice-Boltzmann method for fluid dynamics: basic concept. *Phys. Rev. E* **58**, 3955–3963.
- CHEN, H., CHEN, S. & MATTHAEUS, W. 1992 Recovery of the Navier–Stokes equations using a lattice-gas Boltzmann method. *Phys. Rev. A* **45**, 5339–5342.
- CHEN, H., KANDASAMY, S., ORSZAG, S., SHOCK, R., SUCCI, S. & YAKHOT, V. 2003 Extended Boltzmann kinetic equation for turbulent flows. *Science* **301**, 633–636.
- CHEN, H., TEIXEIRA, C. & MOLVIG, K. 1997 Digital physics approach to computational fluid dynamics: some basic theoretical features. *Intl J. Mod. Phys. C* **8**, 675–684.
- CHEN, H., TEIXEIRA, C. & MOLVIG, K. 1998 Realization of fluid boundary conditions via discrete Boltzmann dynamics. *Intl J. Mod. Phys. C* **9**, 1281–1292.
- CHEN, S., CHEN, H., MARTINEZ, D. & MATTHAEUS, W. 1991 Lattice Boltzmann model for simulation of magnetohydrodynamics. *Phys. Rev. Lett.* **67**, 3776–3779.
- CHEN, S. & DOOLEN, G. 1997 Lattice Boltzmann method for fluid flows. *Annu. Rev. Fluid Mech.* **30**, 329–364.
- COLLINS, W. & DENNIS, C. 1973a The initial flow past an impulsively started circular cylinder. *Q. J. Mech. Appl. Maths* **26**, 53–75.
- COLLINS, W. & DENNIS, S. 1973b Flow past an impulsively started circular cylinder. *J. Fluid Mech.* **60**, 105–127.
- COUTANCEAU, M. & BOUARD, R. 1977a Experimental determination of the main features of the viscous flow in the wake of a circular cylinder in uniform translation. Part 1. Steady flow. *J. Fluid Mech.* **79**, 231–256.
- COUTANCEAU, M. & BOUARD, R. 1977b Experimental determination of the main features of the viscous flow in the wake of a circular cylinder in uniform translation. Part 2. Unsteady flow. *J. Fluid Mech.* **79**, 257–272.
- FILIPPOVA, O. & HANEL, D. 1998 Boundary-fitting and local grid refinement for Lattice-BGK model. *Intl J. Mod. Phys. C* **147**, 1271–1279.
- FORNBERG, B. 1980 A numerical study of steady viscous flow past a circular cylinder. *J. Fluid Mech.* **98**, 819–855.
- FRISCH, U., HASSLACHER, B. & POMEAU, Y. 1986 Lattice-gas automata for the Navier–Stokes equations. *Phys. Rev. Lett.* **56**, 1505–1508.
- GAD-EL-HAK, M. 1999 The fluid mechanics of microdevices – the Freeman Scholar lecture. *J. Fluid Engng* **121**, 5–33.
- GINZBURG, I. & D’HUMIÈRES, D. 2003 Multireflection boundary conditions for lattice-Boltzmann models. *Phys. Rev. E* **68**, 066614.
- GUO, Z., SHI, B. & WANG, N. 2000 Lattice BGK model for incompressible Navier–Stokes equation. *J. Comput. Phys.* **165**, 288–306.
- HE, X. & DOOLEN, G. 1997 Lattice Boltzmann method on curvilinear coordinates system: flow around a circular cylinder. *J. Comput. Phys.* **134**, 306–315.
- HOU, S. 1995 Lattice Boltzmann method for incompressible viscous flow. PhD thesis Kansas State University.

- KIDA, T. & KIMURA, K. 1998 Transient flow around an impulsively started two-dimensional circular cylinder by deterministic vortex method. *Comput. Fluid Dyn. J.* **7**, 325–337.
- KOUMOUTSAKOS, P. & LEONARD, A. 1995 High-resolution simulations of the flow around an impulsively started cylinder using vortex methods. *J. Fluid Mech.* **296**, 1–38.
- LOC, T. 1980 Numerical analysis of unsteady secondary vortices generated by an impulsively started cylinder. *J. Fluid Mech.* **100**, 111–128.
- LOC, T. & BOUARD, R. 1985 Numerical solution of the early stage of the unsteady viscous flow around a circular cylinder: a comparison with experimental visualization and measurements. *J. Fluid Mech.* **160**, 93–117.
- MEI, R. & SHYY, W. 1998 On the finite difference-based lattice–Boltzmann method in curvilinear coordinates. *J. Comput. Phys.* **143**, 426–306.
- PERSILLON, H. & BRAZA, M. 1998 Physical analysis of the transition to turbulence in the wake of a circular cylinder by three-dimensional Navier–Stokes simulation. *J. Fluid Mech.* **365**, 23–88.
- PLOUMHANS, P. & WINCKELMANS, G. 2000 Vortex methods for high-resolution simulations of viscous flow past bluff bodies of general geometry. *J. Comput. Phys.* **165**, 354–406.
- QIAN, Y., D’HUMIÈRES, D. & LALLEMAND, P. 1992 Lattice BGK models for the Navier–Stokes equation. *Europhys. Lett.* **17**, 479–484.
- SCHLICHTING, H. & GERSTEN, K. 2000 *Boundary Layer Theory*, 8th edn. Springer.
- SCHNEIDER, K. & FARGE, M. 2002 Adaptive wavelet simulation of a flow around an impulsively started cylinder using penalisation. *Appl. Comput. Harmonic Anal.* **12**, 374–380.
- SHOCK, R., MALLICK, S., CHEN, H., YAKHOT, V. & ZHANG, R. 2002 Recent simulation results on 2D NACA airfoils using a lattice-Boltzmann based algorithm. *AIAA J. Aircraft* **39**, 434–439.
- SHOCK, R., QIAN, Y., CHEN, H. & ZHANG, R. 2002 PowerFLOW simulations for 2D cavity and backward step flows. *Exa Internal Paper*.
- SMITH, P. & STANSBY, P. 1988 Impulsively started flow around a circular cylinder by the vortex method. *J. Fluid Mech.* **194**, 45–77.
- WANG, X. & DALTON, C. 1991 Numerical solution for impulsively started and decelerated viscous flow past a circular cylinder. *Intl J. Numer. Meth. Fluids* **12**, 383–400.